



OGLE-2018-BLG-0022: A Nearby M-dwarf Binary

R. A. Street¹ , E. Bachelet¹, Y. Tsapras², M. P. G. Hundertmark², V. Bozza³, M. Dominik⁴
ROME/REA and MiNDSTeP Teams

ROME/REA Team,

and

D. M. Bramich⁵, A. Cassan⁶, K. Horne⁴ , S. Mao^{7,8}, A. Saha⁹, J. Wambsganss^{2,10}, Weicheng Zang⁷

MiNDSTeP Team,

U. G. Jørgensen¹¹, P. Longa-Peña¹², N. Peixinho¹³, S. Sajadian¹⁴, M. J. Burgdorf¹⁵, J. Campbell-White¹⁶, S. Dib¹⁷, D. F. Evans¹⁸,
Y. I. Fujii^{19,20}, T. C. Hinse²¹, E. Khalouei²², S. Lowry¹⁶, S. Rahvar²², M. Rabus^{23,24,25,26}, J. Skottfelt²⁷, C. Snodgrass^{28,29},
J. Southworth¹⁸, and J. Tregloan-Reed¹²

¹ LCOGT, 6740 Cortona Drive, Suite 102, Goleta, CA 93117, USA; rstreet@lco.global

² Zentrum für Astronomie der Universität Heidelberg, Astronomisches Rechen-Institut, Mönchhofstr. 12-14, 69120 Heidelberg, Germany

³ Dipartimento di Fisica “E.R. Caianiello,” Università di Salerno, Via Giovanni Paolo II 132, 84084, Fisciano, Italy

⁴ Centre for Exoplanet Science, SUPA, School of Physics & Astronomy, University of St Andrews, North Haugh, St Andrews KY16 9SS, UK

⁵ New York University Abu Dhabi, Saadiyat Island, Abu Dhabi, P.O. Box 129188, United Arab Emirates

⁶ Institut d’Astrophysique de Paris, Sorbonne Université, CNRS, UMR 7095, 98 bis boulevard Arago, 75014 Paris, France

⁷ Physics Department and Tsinghua Centre for Astrophysics, Tsinghua University, Beijing 100084, People’s Republic of China

⁸ National Astronomical Observatories, Chinese Academy of Sciences, 20A Datun Road, Chaoyang District, Beijing 100012, People’s Republic of China

⁹ National Optical Astronomy Observatory, 950 North Cherry Avenue, Tucson, AZ 85719, USA

¹⁰ International Space Science Institute (ISSI), Hallerstraße 6, 3012 Bern, Switzerland

¹¹ Niels Bohr Institute & Centre for Star and Planet Formation, University of Copenhagen, Øster Voldgade 5, 1350 Copenhagen, Denmark

¹² Unidad de Astronomía, Universidad de Antofagasta, Av. Angamos 601, Antofagasta, Chile

¹³ CITEUC—Center for Earth and Space Research of the University of Coimbra, Geophysical and Astronomical Observatory, R. Observatorio s/n, 3040-004 Coimbra, Portugal

¹⁴ Department of Physics, Isfahan University of Technology, Isfahan 84156-83111, Iran

¹⁵ Universität Hamburg, Faculty of Mathematics, Informatics and Natural Sciences, Department of Earth Sciences, Meteorological Institute, Bundesstraße 55, 20146 Hamburg, Germany

¹⁶ Centre for Astrophysics & Planetary Science, The University of Kent, Canterbury CT2 7NH, UK

¹⁷ Max Planck Institute for Astronomy, Königstuhl 17, D-69117, Heidelberg, Germany

¹⁸ Astrophysics Group, Keele University, Staffordshire, ST5 5BG, UK

¹⁹ Department of Physics, Nagoya University, Furo-cho, Chikusa-ku, Nagoya, 464-8602, Japan

²⁰ Institute for Advanced Research, Nagoya University, Furo-cho, Chikusa-ku, Nagoya, 464-8601, Japan

²¹ Chungnam National University, Department of Astronomy and Space Science, 34134 Daejeon, Republic of Korea

²² Department of Physics, Sharif University of Technology, P.O. Box 11155-9161 Tehran, Iran

²³ Instituto de Astronomía, Facultad de Física, Pontificia Universidad Católica de Chile, casilla 306, Santiago 22, Chile

²⁴ Max-Planck-Institut für Astronomie, Königstuhl 17, D-69117 Heidelberg, Germany

²⁵ LCOGT, 6740 Cortona Drive, Suite 102, Goleta, CA 93111, USA

²⁶ Department of Physics, University of California, Santa Barbara, CA 93106-9530, USA

²⁷ Centre for Electronic Imaging, Department of Physical Sciences, The Open University, Milton Keynes, MK7 6AA, UK

²⁸ School of Physical Sciences, Faculty of Science, Technology, Engineering and Mathematics, The Open University, Walton Hall, Milton Keynes, MK7 6AA, UK

²⁹ Institute for Astronomy, University of Edinburgh, Royal Observatory, Edinburgh EH9 3HJ, UK

Received 2019 January 31; revised 2019 March 6; accepted 2019 March 14; published 2019 May 7

Abstract

We report observations of the binary microlensing event OGLE-2018-BLG-0022, provided by the Robotic Observations of Microlensing Events (ROME)/Reactive Event Assessment (REA) Survey, which indicate that the lens is a low-mass binary star consisting of M3 ($0.375 \pm 0.020 M_{\odot}$) and M7 ($0.098 \pm 0.005 M_{\odot}$) components. The lens is unusually close, at 0.998 ± 0.047 kpc, compared with the majority of microlensing events, and despite its intrinsically low luminosity, it is likely that adaptive optics observations in the near future will be able to provide an independent confirmation of the lens masses.

Key words: binaries: general – gravitational lensing: micro – techniques: photometric

1. Introduction

Microlensing offers a way to explore the populations of stellar and planetary systems in regions of the Galaxy where they are too faint to study via alternative techniques, and at orbital separations where reflex-based and transit methods are inefficient. Seventy-two planetary systems discovered by their lensing signature have been published to date³⁰ but notably

the method is also sensitive to many other intrinsically low-luminosity objects, including late-type stars and brown dwarfs as well as compact objects, including white dwarfs and black holes (Wyrzykowski et al. 2016), since the technique depends on the gravity, rather than the light, from the lensing system.

A microlensing event occurs when a foreground object crosses the observer’s line of sight to an unrelated luminous source in the background, causing the latter to brighten and fade as the objects move into and out of alignment. Since the

³⁰ Source: NASA Exoplanet Archive, <https://exoplanetarchive.ipac.caltech.edu/>.

events are transient, occurring unpredictably³¹ but still for a relatively limited sample of stars and without repetition, surveys typically maximize their yield by photometric monitoring of densely populated regions of the Galactic bulge, where the microlensing optical depth, or probability of lensing is greatest, $\Gamma = [18.74 \pm 0.91] \times 10^{-6} \exp[(0.53 \pm 0.05)(3-|b|)] \text{ star}^{-1} \text{ yr}^{-1}$ for $|l| < 5^\circ$ (Sumi & Penny 2016), resulting in ~ 2000 events being discovered per year, of which $\sim 10\%$ are due to binary lenses. While the guiding scientific goal of most of these surveys is generally the discovery of exoplanets, they yield binary lens systems with a wide range of mass ratios, all of which must be carefully observed and assessed to determine the true nature of the lensing system.

Here we present multiband observations of the microlensing event OGLE-2018-BLG-0022 from the new Robotic Observations of Microlensing Events (ROME)/Reactive Event Assessment (REA) Survey, along with a description of the analysis process. In the next section, we outline the essential theoretical model parameters and our motivation for this observing strategy, followed by a brief description of the ROME/REA project and observations of this event. The light curve modeling and analyses are presented in Sections 5 and 6 and we discuss their implications for the nature of the lens in Section 7.

2. Characterizing Microlensing Events

A foreground lensing object of mass M_L , at distance D_L from the observer, deflects the light from a background source at distance D_S with a characteristic angular radius, $\theta_E = \sqrt{\frac{4GM_L D_{LS}}{c^2 D_L D_S}}$ (Refsdal 1964), where D_{LS} is the distance between the lens and source. As the relative proper motion, μ_{rel} , of the lens and source narrows their projected angular separation $u(t)$ to a minimum u_0 at time t_0 , the source appears magnified as a function of time, with the magnification given by $A(t) = \frac{u^2 + 2}{u\sqrt{u^2 + 4}}$. Microlensing events have a characteristic Einstein crossing time, t_E , defined as the time taken for the source to cross θ_E in a lens-centered geometry.

At their simplest, single, point-lens microlensing events are described by just three parameters, t_0 , u_0 , t_E , and binary lenses require just three more: the mass ratio of the lens components, $q = M_{L,2}/M_{L,1}$, their angular separation, s , normalized by θ_E and α , and the counterclockwise angle between the binary axis and the source trajectory.

All of these parameters may be measured directly from time-series photometry in a single passband, but unfortunately this alone does not reveal the physical nature of the lens, since θ_E has a mass–distance degeneracy (Dominik 1999). This ambiguity is most commonly broken by measuring two effects.

The motion of the observer during the event requires a modification of $u(t)$ to take microlensing parallax, $\pi_E = (\pi_{E,N}, \pi_{E,E})$, into account. This may be measured as a skew in the light curve of events with $t_E \gtrsim 30$ days, or otherwise by combining simultaneous light curves from widely separated observers, such as on Earth and in space (e.g., Dong et al. 2007; Shvartzvald et al. 2016). Although both the lens and source may be kiloparsecs distant from the observer, the finite angular size of the latter can nevertheless introduce detectable distortions around the peak of the light curve, parameterized as

$\rho = \theta_S/\theta_E$. ρ can then be used to determine θ_E , if an independent measurement is made of the angular radius of the source θ_S .

As microlensing sources are typically faint, with $I \gtrsim 15.0$ mag, their angular sizes are most easily estimated from stellar models based on their spectral type. This is usually constrained from a low-cadence light curve of the event in a second optical bandpass, since the microlensing magnification can be used to distinguish the light from the source from other stars blended within the same point-spread function (PSF). Ongoing microlensing surveys, such as the Optical Gravitational Lensing Experiment (OGLE³²; Udalski et al. 1992), Microlensing Observations in Astrophysics (MOA³³; Bond et al. 2001; Sumi et al. 2003; Sako et al. 2008), and Korea Microlensing Telescope Network (KMTNet; Park et al. 2012), typically obtain imaging data in two broadband filters, usually Bessell- V , I . Priority is given to I -band observations in order to properly constrain all light curve features, with V -band data obtained at a much lower and variable cadence.

3. The ROME/REA Project

The goal of the ROME/REA Microlensing Project (described in Y. Tsapras et al. 2019, in preparation) is to ensure that the source stars of microlensing events within its footprint are well characterized and hence that the physical nature of the lensing objects can be determined. The project has adopted a novel observing strategy designed to complement those of the existing surveys, which combines both regular survey-mode observations (ROME) in three passbands with higher cadence single-filter (REA) observations obtained around the event peaks, or in response to caustic crossings. This strategy takes advantage of the multiple 1 m telescopes at each site of the Las Cumbres Observatory (LCO) telescope network and the flexibility offered by the network’s robotic scheduling system (Saunders et al. 2014).

The ROME survey monitors 20 selected fields in the Galactic bulge where the rate of microlensing events is highest (Sumi & Penny 2016). The field of view of each pointing is $26' \times 26'$, determined by the field of the *Sinistro* cameras of the LCO 1 m network, giving a total survey footprint of 3.76 sq. deg. A triplet of 300 s exposures in SDSS- g' , $-r'$, and $-i'$ are obtained in each survey visit to a field, and all 20 fields are surveyed with a nominal cadence of once every 7 hr thanks to the geographic distribution of the LCO network (Brown et al. 2013). Specifically, ROME/REA uses the LCO southern ring of identical 1 m telescopes at Cerro Tololo Inter-American Observatory (CTIO), Chile, the South African Astronomical Observatory (SAAO), and South Africa and Siding Spring Observatory (SSO), Australia. ROME survey observations are therefore conducted around the clock, as long as the fields are visible from each site, between April 1 to October 31 each year, starting in 2017.

As such, the ROME survey was designed to complement other ongoing surveys, by improving the color data available to characterize microlensing source stars and filling a gap between the surveys that observe the bulge at high cadence but predominantly in a single filter and very wide-field surveys that obtain multibandpass data but sometimes at a cadence that is too low to provide useful constraints to microlensing events.

³¹ We note that astrometry from the *Gaia* mission has recently enabled some events to be predicted in advance (Bramich 2018).

³² <http://ogle.astrouw.edu.pl/>

³³ <http://www.phys.canterbury.ac.nz/moa/>

Table 1
Summary of Telescopes and Instruments Used

Obs. Mode	Site	Telescope	Camera	Filters
ROME	Chile	Dome C, 1m0-04	f03	i'
ROME	Chile	Dome A, 1m0-05	f15	g', r', i'
ROME	South Africa	Dome A, 1m0-10	f16	g', r', i'
ROME	South Africa	Dome C, 1m0-12	f06	r', i'
ROME	Australia	Dome A, 1m0-11	f12	g', r', i'
REA	Chile	Dome A, 1m0-05	f15	g', r', i'
REA	Chile	Dome C, 1m0-04	f03	i'
REA	South Africa	Dome A, 1m0-10	f16	i'
REA	South Africa	Dome C, 1m0-12	f06	r', i'
REA	Australia	Dome A, 1m0-11	f12	g', r', i'
REA	Australia	Dome B, 1m0-03	f11	i'
MiNDSTeP	Chile	1.54 m	EMCCD	i_{DK}
Total number of images				1260

For example, OGLE and KMTNet obtain data in V at <1 day cadence but I -band data at intervals <15 minutes, while the Zwicky Transient Factory observes the northern plane nightly in SDSS- r and occasionally in SDSS- g . ROME/REA complements the wavelength coverage of the wavelength coverage of the near-infrared United Kingdom InfraRed Telescope (UKIRT; Shvartzvald et al. 2017) and VISTA Variables in The Via Lactea (VVV) surveys (Minniti et al. 2010).

4. Observations and Data Reduction

The event OGLE-2018-BLG-0022 was first discovered and classified as a microlensing event by OGLE on 2018 February 7, and subsequently re-identified by the same survey as OGLE-2018-BLG-0052 on 2018 February 21. The same object was also independently discovered by MOA on 2018 February 25, who assigned the label MOA-2018-BLG-031.

With R.A., decl. coordinates of 17:59:27.04, $-28:36:37.00$ (J2000.0), this event lies within the boundaries of ROME-FIELD-16. ROME observations of this field began on 2017 March 18 using the LCO facilities summarized in Table 1. In general, we endeavored to conduct ROME and REA observations using a consistent set of cameras at the three sites in order to limit the number of data sets and any calibration offsets between them, so the majority of our data was provided by three instruments. However, the LCO network is designed to optimize its schedule globally by moving observation requests between telescopes, and REA-mode observations in particular were obtained from multiple cameras for this reason. Over the longer term, it was also necessary occasionally to transfer ROME observations between telescopes at the same site, when technical issues affected the original instruments. Nevertheless, all data were obtained using the *Sinistro* class of optical cameras, all of which consist of $4k \times 4k$ Fairchild CCDs operated in bin 1×1 mode with a pixel scale of $0''.389 \text{ pix}^{-1}$.

On 2018 March 13 the ARTEMiS anomaly detection system (Dominik et al. 2008) found that the light curve of the event was deviating from a point-source, point-lens model on the rising section of its light curve, and subsequent modeling efforts by Bozza, Cassan, Bachelet, and Hirao³⁴ confirmed that the event was most likely caused by a binary lens. As the event brightened toward its peak magnification it met the criteria for REA and our RoboTAP target prioritization software

(Hundertmark et al. 2018) began to schedule REA-mode observations in addition to those for ROME. The models provided by V. Bozza’s RTModel system for real-time analysis (Bozza 2010) provided predictions regarding the timing of future caustic crossings that were used to plan observations. Following the ROME/REA strategy, REA-LO mode, single-filter observations were automatically requested every hour, while REA-HI observations were triggered to ensure data would be obtained at high cadence (every 15 minutes) for the periods of predicted caustic crossing. Photometry was provided to RTModel from several teams including ROME/REA while the event was in progress, which allowed both the model predictions and the REA observations to be updated accordingly until the event was observed to return to the source’s baseline brightness. REA-mode observations continued until after the peak of the event, ending on 2018 June 10.

All ROME/REA imaging data were preprocessed by the standard LCO *BANZAI* pipeline to remove the instrumental signatures, then reduced using a difference image analysis (DIA) pipeline based on the *DanDIA* package by Bramich (2008) and Bramich et al. (2013) to produce light curve photometry.

Independently of ROME/REA, MiNDSTeP observations with the Danish 1.54 m in Chile were triggered automatically by the SIGNALMEN anomaly detector (Dominik et al. 2007), operated as part of the ARTEMiS system³⁵ (Dominik et al. 2008, 2010), in conjunction with real-time modeling of anomalous events provided by RTModel³⁶ (Bozza et al. 2018). They began on 2018 April 25 and continued until 2018 May 18, with the goal of ensuring high-cadence coverage of the anomaly. These data were obtained with the EMCCD camera equipped with a long-pass filter with a short-wavelength cutoff at 6500 \AA , making the filter function resemble a combined SDSS- i' plus SDSS- z' plus the long-wavelength part of the SDSS- r' filter, denoted as i_{DK} in Table 1. These data were reduced with a version of the *DanDIA* package (Bramich 2008) which has been optimized for the reduction of data from this EMCCD instrument (Skottfelt et al. 2015; Evans et al. 2016).

5. Light Curve Analysis

Some residual structures remained after the initial processing. As the event timescale is relatively long ($t_E > 50$ days), it was likely that annual parallax and, potentially, the orbital motion of the lens may be significant. We therefore explore these two second-order effects and find a great improvement of the model likelihood.

Since the light curve presents clear signatures of a multiple lens, we began by fitting a simple uniform-source binary lens (USBL) model to the light curve data, where both lens and observer were considered to be static, using the pyLIMA modeling package (Bachelet et al. 2017). It should be noted that pyLIMA’s geometric convention is to place the most massive body on the left, and α is defined to be the counterclockwise angle between the binary axis and the source trajectory. Initial model fits indicated significant deviations around the peak that are typically introduced when the angular radius of the source star is non-negligible relative to the angular size of the caustic. We therefore investigated finite-source

³⁴ Private communications.

³⁵ <http://www.artemis-uk.org/>

³⁶ <http://www.fisica.unisa.it/GravitationAstrophysics/RTModel.htm>

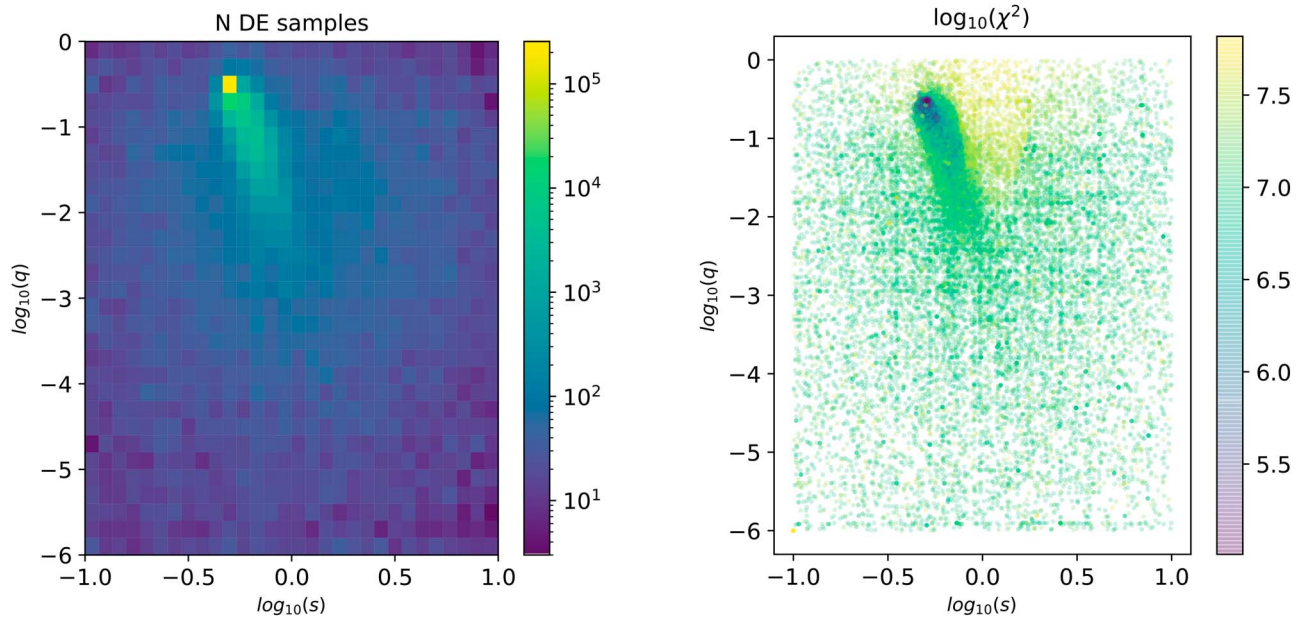


Figure 1. Maps of the $(\log_{10}(s)$ vs. $\log_{10}(q)$) parameter space mapped out by a differential evolution (DE) algorithm. (Left) A 2D histogram of the number of DE samples for each pixel in the parameter space, and (right) a 2D histogram of the chi-square values of each pixel. This plot was downsampled by a factor of 2 without loss of detail to minimize the plot filesize.

Table 2
Linear Limb-darkening Coefficients Used

Facility	Filter	u_λ	Γ_λ
LCO 1 m	SDSS- g'	0.8852	0.8371
LCO 1 m	SDSS- r'	0.7311	0.6445
LCO 1 m	SDSS- i'	0.603	0.503
Danish	i_{DK}	0.5139	0.4134

binary lens (FSBL) models, and took the limb-darkening of the source into account when computing the magnification of the source. A linear limb-darkening model is commonly sufficient for microlensing models, and we adopt the widely used formalism (Albrow et al. 1999)

$$I_\lambda = \frac{F_\lambda}{\pi\theta_*^2} \left[1 - \Gamma_\lambda \left(1 - \frac{3}{2} \cos \phi \right) \right], \quad (1)$$

where I_λ is the intensity of the source at wavelength, λ , F_λ is the total flux from the source in a given passband, and ϕ is the angle between the line of sight to the observer and the normal to the stellar surface. The limb-darkening coefficient, Γ_λ , is related to the u_λ limb-darkening coefficients derived from the ATLAS stellar atmosphere models presented (Claret & Bloemen 2011) by the expression

$$\Gamma_\lambda = \frac{2u_\lambda}{3 - u_\lambda}. \quad (2)$$

The values of u_λ and Γ_λ applied for each data set are presented in Table 2.

The PSF naturally differs between data sets acquired from different observing sites and instruments. In the crowded star fields of the Galactic bulge, the PSF of the source star is highly likely to be blended with those of neighboring stars. The measured flux of the target at time t in data set k , $f(t, k)$ is calculated as a function of lensing magnification, $A(t)$, $f(t, k) = A(t)f_s(k) + f_b(k)$. Here, $f_s(k)$ is the flux of the source star and

$f_b(k)$ represents the flux of all stars blended with the source in the data set. A regression fit was performed in the course of the modeling process to measure f_s and f_b for each data set.

pyLIMA's differential evolution (DE; Storm & Price 1997) solution-finding algorithm was used to explore parameter space and zero in the region that best represents the data, after which we mapped the posterior distribution of each region using a Monte-Carlo Markov Chain (MCMC) algorithm (emcee; Foreman-Mackey et al. 2013). Once the parameter space minimum had been localized, the best-fitting model parameters were identified using the Levenberg–Marquardt algorithm (Levenberg 1944; Marquardt 1963) or the trust region reflective algorithm (Coleman & Li 1994; Branch et al. 1999).

The DE algorithm was initially given as few restrictions as possible (t_0 to lie within ± 50 days of the event peak; $-0.3 \leq u_0 \leq 0.3$) so that it would explore a wide parameter space and identify all possible minima for further study. The DE algorithm outputs the fit parameters for each candidate solution, which can be used to map the parameter space as shown in Figure 1. By design, the algorithm returns more solutions in regions where χ^2 minima are located, so a 2D histogram of the number of solutions per element of $\log_{10}(s)$ versus $\log_{10}(q)$ space indicates where solutions lie and further investigation is required. This exploration indicated a single but extended minimum, and consistently converged on solutions where the source-lens relative trajectory intersected the central caustic. The origin of the coordinate system was set to that of the central caustic during the modeling process, for increased stability of fit, so the impact parameter u_c is measured relative to this point.

Before refining the model, we reviewed the photometric uncertainties for all light curves. All photometry suffers from systematic noise at some level, and this must be quantified to avoid over-fitting the data. pyLIMA provides statistical tests of the goodness-of-fit, including a Kolmogorov–Smirnov test, an Anderson–Darling test, and a Shapiro–Wilk test (Bachelet et al. 2015). If the p -value returned by tests was $< 1\%$, the

Table 3
Coefficients Used in the Rescaling of Photometric Uncertainties for Each Data Set and Filter

Facility	g'		r'		i'		i_{DK}	
	a_0	a_1	a_0	a_1	a_0	a_1	a_0	a_1
Chile, Dome A, fl15	0.0	1.0	0.0	1.0	0.0	1.0
Chile, Dome C, fl03	0.0	1.0
South Africa, Dome A, fl16	0.047 ± 0.03	1.0	0.0	1.0	0.019 ± 0.004	2.874 ± 1.597
South Africa, Dome C, fl06	0.0	1.0	0.0	1.0
Australia, Dome A, fl12	0.0	1.0	0.0	1.0	0.0	2.445 ± 0.831
Australia, Dome B, fl11	0.0	1.0
Danish, 1.54, m, DFOSC	0.0	1.0

Table 4
Parameters of the Best-fitting Close-binary Models

Parameter	Static binary	Binary+parallax	Binary+parallax+orbital motion	
	USBL	USBL	USBL	FSBL
t_0 [HJD]	2458239.52808	2458239.98991	2458239.95128	2458240.02326
	0.00317	0.00326	0.00357	0.00381
u_c	0.004421	0.004496	0.004426	0.004526
	0.000017	0.000015	0.000019	0.000017
t_E [days]	72.767	70.417	74.905	75.917
	0.065	0.069	0.051	0.071
ρ	0.004207	0.004357	0.003967	0.004021
	0.000011	0.000013	0.000089	0.000012
$\log_{10}(s)$	-0.29528	-0.27221	-0.27748	-0.27484
	0.00017	0.00016	0.00023	0.00018
$\log_{10}(q)$	-0.48924	-0.56329	-0.58343	-0.59851
	0.00030	0.00033	0.00024	0.00042
α [radians]	2.97536	2.95992	2.96006	2.95522
	0.00032	0.00026	0.00034	0.00031
$\pi_{E,N}$		0.5008	0.4718	0.4841
		0.0021	0.0015	0.0030
$\pi_{E,E}$		0.0852	0.0664	0.069933
		0.0022	0.0018	0.0031
$\frac{ds}{dt}$ [θ_E /year]			0.001158	0.001552
			0.000039	0.000040
$\frac{d\alpha}{dt}$ [radians/year]			-0.000016	-0.000442
			0.000038	0.000043
χ^2	16884.06	7239.03	6863.32	6979.39
$\Delta\chi^2$		-9645.03	-375.71	116.07

Note. Uncertainties are indicated in the second line for each parameter. $\Delta\chi^2$ is calculated from the difference in χ^2 between the each fit and the fit in its neighboring column to the left.

uncertainties on each data set were revised, which was necessary in all cases.

Following common practice (e.g., Skowron et al. 2015), we renormalized the photometric errors, $\sigma(k)$, of each data set, k , according to the expression (in magnitude units)

$$\sigma(k)' = \sqrt{a_0^2(k) + a_1^2(k)\sigma(k)^2}. \quad (3)$$

The coefficients $a_0(k)$, $a_1(k)$ were estimated by requiring that the reduced $\chi_{\text{red}}^2 = 1$. If the fit could not be constrained then the coefficients were set to 0.0 and 1.0, respectively. This could occur for a variety of reasons, the most common being that the majority of measurements in a given data set were taken primarily over the peak of the event, where the rescaling fit was heavily influenced by residuals from the model, particularly around caustic crossings. This was mitigated to some degree by iterating the model fitted with the rescaling process, to verify

that the uncertainties of specific data points were not being excessively scaled. A second problem was that the photometric uncertainties for a given data set spanned a relatively short numerical range, leading to instability in the linear regression fit of the above function, and resulting in statistically nonsensical coefficients. Lastly, for some data sets the residual scatter in the photometry was accurately represented by the uncertainties, implying that no rescaling was required. The adopted values are given in Table 3.

As there are both wide- and close-binary configurations that can produce very similar caustic structures (the well-documented close-wide degeneracy; Dominik 1999, 2009), we split the parameter space into two regions, $s > 1$ and $s < 1$, which were explored separately. For this event, the close-binary solutions proved to be a significantly better fit than the wide-binary models; the parameters of the best-fitting models in each case

Table 5
Parameters of the Best-fitting Wide-binary Models

Parameter	Static binary	Binary+parallax	Binary+parallax +orbital motion
	USBL	USBL	USBL
t_0 [HJD]	2458238.66632 0.00373	2458239.19101 0.00352	2458240.07697 0.04935
u_c	-0.002834 0.000015	-0.003548 0.0000099	-0.006768 0.000027
t_E [days]	129.3778 0.0072	101.455 0.091	122.516 0.107
ρ	0.002042 0.000020	0.002514 0.0000060	0.0025865 0.0000090
$\log_{10}(s)$	0.578942 0.000026	0.51043 0.00013	0.44685 0.00037
$\log_{10}(q)$	-0.00065 0.00036	-0.13962 0.00063	-0.33554 0.00098
α [radians]	-3.01041 0.00016	-2.99934 0.00023	-1.89562 0.00132
$\pi_{E,N}$		-0.28192 0.00077	-0.48863 0.00315
$\pi_{E,E}$		0.1125 0.0011	-0.3915 0.0018
$\frac{ds}{dt}$ [θ_E /year]			-0.022095 0.000044
$\frac{d\alpha}{dt}$ [radians/ year]			-0.007852 0.000013
χ^2	36501.669	20519.11	8141.82
$\Delta\chi^2$		-15982.56	-12377.29

Note. Uncertainties are indicated in the second line for each parameter. $\Delta\chi^2$ is calculated from the difference in χ^2 between the each fit and the fit in its neighboring column to the left.

are presented in Tables 4–5. We found a significant improvement in χ^2 was achieved by including microlensing parallax, which is expected for an event of this duration, and also lens binary orbital motion.

At each stage of modeling, as these effects were included, we explored FSBL models as well as USBL models. While the best-fitting of these models indicated similar parameters to the USBL models, their χ^2 values were found to be somewhat higher. A close examination of the residuals showed that this is driven by a small number (5) of data points around the caustic crossing at 2458232.7, where the model is most sensitive to the limb-darkening of the source star. Two of the data points are in SDSS- g' band and three are in SDSS- i' , which in principle might provide an independent constraint on Γ . Regrettably, the caustic crossing occurred between the end of the night in Chile and the start of the night in Australia, and the data points were obtained from different instruments, under different conditions. This is a situation where residual systematic noise in the photometry can easily exceed the finite source signature, so proceeding with finite-source models was judged to be unsafe.

Figure 2 displays the light curve data overlaid with the best-fitting model, a uniform-source close-binary lens, and a plot of the source’s trajectory relative to the lens plane and caustic structures is shown in Figure 3. We note that there is a second degeneracy: lens-source relative trajectories with a negative u_c value could in principle produce a very similar light curve. These solutions were allowed during our fitting process, but

were always disfavored in the results. This would not strongly impact the physical characteristics of the lens inferred from the best-fit model.

6. Source Color Analysis

We adopted data from Chile, Dome A, camera f115 to act as our photometric reference, since this site consistently has the best observing conditions of the whole network. After reviewing all available data, a trio of single g' , r' , i' images taken sequentially on 2017 July 26 between 04:05 and 04:17 UTC were selected as the reference images for these data sets because they were obtained in the best seeing, transparency, and sky background conditions. These images were used as the reference images for the DIA pipeline. PSF fitting photometry was conducted on the same images, in order to determine the reference fluxes of all detected stars.

The positions of all detected stars (as determined from the world coordinate system fit, WCS, for each image) were cross-matched against the VPHAS+ catalog (Drew et al. 2014), from which calibrated SDSS- g , $-r$, and $-i$ magnitudes were extracted. To mitigate the impact of differential extinction across the field of view, stars within 2 arcmin of the lensed star were selected for the purpose of measuring the photometric transformation from LCO instrumental magnitudes to the VPHAS+ system. Color–magnitude diagrams from the ROME data are presented in Figure 4.

While this procedure provides an approximate photometric calibration, fields in the Galactic bulge suffer from high extinction, which is often spatially variable across the field of view of a single ROME exposure. To account for this, it has become standard practice in microlensing to measure the offset of the red clump from its expected magnitude and color.

Red clump giant stars are often used as standard candles, since their absolute luminosity is constant, being relatively insensitive to changes in metallicity and age, and they occur with high frequency across the Galactic plane. Recently, Ruiz-Dern et al. (2018) summarized red clump photometric properties in a wide range of photometric systems, including their absolute magnitudes in the SDSS passbands: $M_{g,RC,0} = 1.331 \pm 0.056$ mag, $M_{r,RC,0} = 0.552 \pm 0.026$ mag, $M_{i,RC,0} = 0.262 \pm 0.032$ mag.

To determine the apparent magnitude and colors of the red clump stars, we assume that they are located in the Galactic bar. Nataf et al. (2013) indicated that the Galactic bar is orientated at a viewing angle of $\phi_{\text{Bar}} = 40^\circ$, meaning that the distance to the red clump, D_{RC} , is a function of Galactic longitude, l :

$$\frac{R_0}{D_{\text{RC}}} = \frac{\sin \phi_{\text{Bar}} + l}{\phi_{\text{Bar}}} = \cos l + \sin l \cot \phi_{\text{Bar}}, \quad (4)$$

where $R_0 = 8.16$ kpc (we note that the bar angle may be somewhat smaller; Cao et al. 2013; Wegg & Gerhard 2013; but this will cause only small changes to the results). Based on the location of OGLE-2018-BLG-0022 in Galactic coordinates $(l, b) = (1.82295, -2.44338)^\circ$, the distance to the red clump in this field is estimated to be 7.87 kpc. We used this to estimate the apparent photometric properties (denoted by $m_{\lambda,RC,0}$ for different passbands, λ) summarized in Table 6.

The red clump is clearly identifiable in the ROME color–magnitude diagrams (Figure 4). Stars within 2 arcmin of the target were used to measure the centroid of the clump in magnitude and color by applying the following selection cuts: $15.5 \leq i \leq 16.5$ mag, $16.2 \leq r \leq 17.5$ mag, $17.8 \leq g \leq$

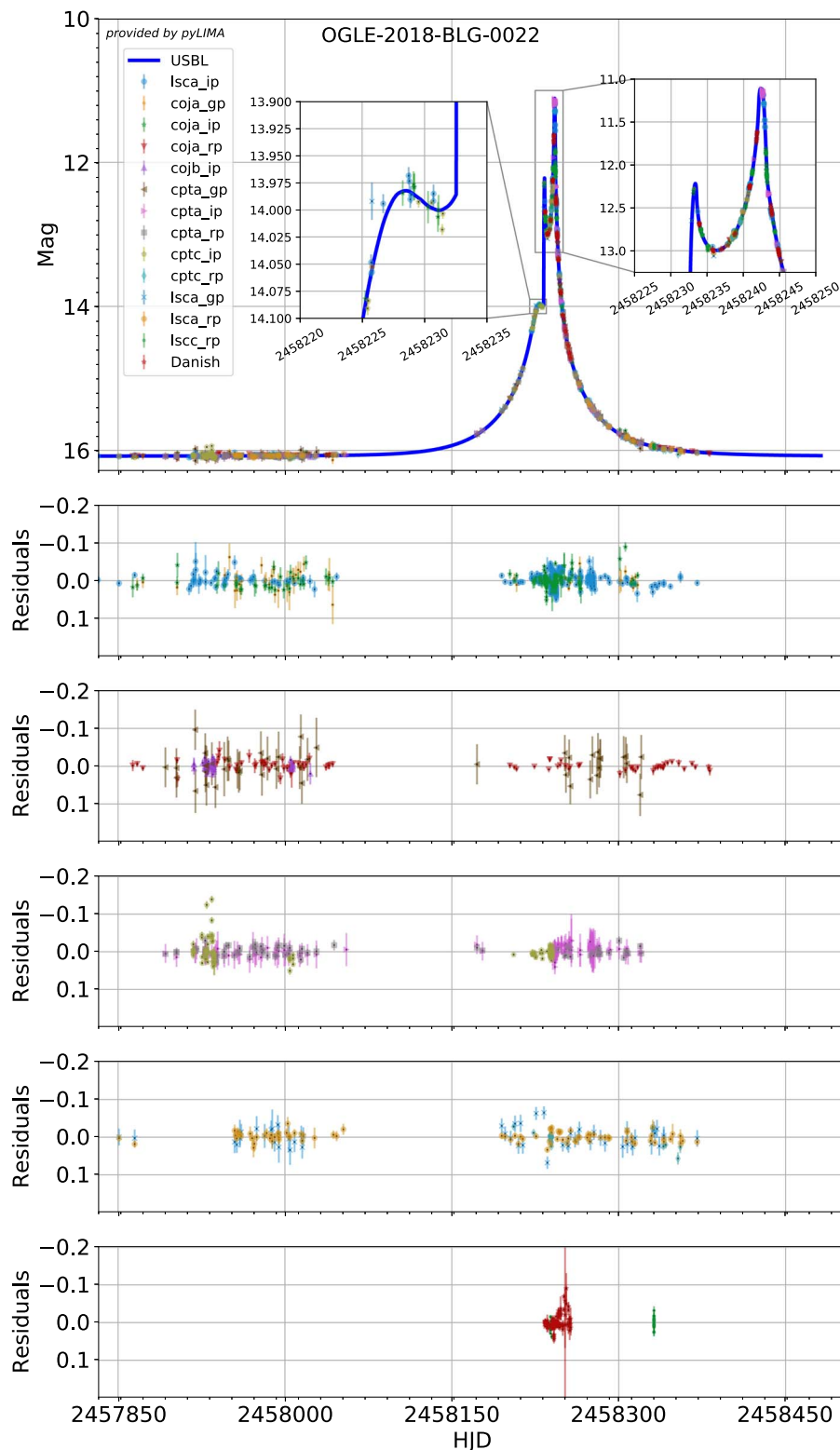


Figure 2. Plot of all photometric data sets overlaid with the best-fitting USBL model light curve including parallax and orbital motion. The inset in the top panel shows the light curve during the caustic crossing in more detail. The bottom panel displays the photometric residuals once the model is subtracted from the data.

19.5 mag, $0.8 \leq (r - i) \leq 1.2$ mag, $1.5 \leq (g - r) \leq 2.2$ mag. The measured centroids of the red clump are presented in Table 6.

The offset of the red clump from its expected photometric properties was used to estimate the extinction, A_λ , and

reddening, $E(\text{color})$ for the red clump along the line of sight to the target.

These quantities were then used to correct the photometric properties of the source and blend, as derived from the best-fitting light curve model, assuming that they have the same

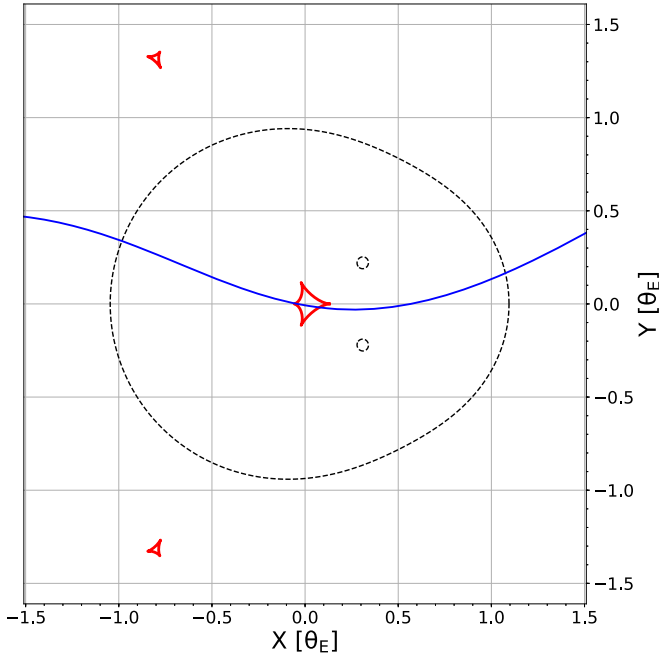


Figure 3. Plot of the lens plane in a lens-centric geometry, showing the caustic structures for the binary lens in red in relation to the source-lens relative trajectory in blue. The dotted black lines represent the critical curve.

extinction and reddening as the red clump. The resulting data are summarized in Table 7.

We note that the ROME survey strategy provides useful means to verify the source flux determined from the model. Since ROME observations are always conducted as a sequence of back-to-back (g' , r' , i') exposures taken within ~ 15 minutes of each other, the magnification of the event can normally be taken to be approximately the same for all three images in a trio (excluding caustic crossings). These observations can be used to measure the source color and blend flux independently of the model, as follows. The total flux measured in a given passband λ , f_λ consists of the source flux, $f_{s,\lambda}$, multiplied by the lensing magnification, A , combined with the flux from any other blended stars along the line of sight, $f_{b,\lambda}$: $f_\lambda(t) = f_{s,\lambda} A(t) + f_{b,\lambda}$. Contemporaneous fluxes in multiple passbands can be combined as

$$f_{\lambda,1}(t) = \frac{f_{s,\lambda,1}}{f_{s,\lambda,2}}(f_{\lambda,2}(t) - f_{b,\lambda,2}) + f_{b,\lambda,1}. \quad (5)$$

This allows the source color to be measured by linear regression from the slope of the fluxes in different passbands, plotted against one another. Applying this technique, we measured $(g-r)_s = 2.115 \pm 0.007$ mag, $(g-i)_s = 3.253 \pm 0.007$ mag, $(r-i)_s = 1.138 \pm 0.002$ mag. These values are consistent with the colors determined from the model-predicted source fluxes in Table 7. The resulting time series of source color measurements are shown in Figure 4, and can be evaluated relative to the crosshairs indicating the source color measured from the light curve analysis.

The source star's location on the color-color diagram (Figure 5) was compared with theoretical stellar isochrones derived from the PARSEC model³⁷ (Bressan et al. 2012) for solar metallicity and ages ranging from 3.98×10^6 to

³⁷ <http://stev.oapd.inaf.it/cgi-bin/cmd>

Table 6
Photometric Properties of the Red Clump, with Absolute Magnitudes (M_λ) Taken from Ruiz-Dern et al. (2018), and the Measured Properties from ROME Data

$M_{g,RC,0}$	1.331 ± 0.056 mag
$M_{r,RC,0}$	0.552 ± 0.026 mag
$M_{i,RC,0}$	0.262 ± 0.032 mag
$(g-r)_{RC,0}$	0.779 ± 0.062 mag
$(g-i)_{RC,0}$	1.069 ± 0.064 mag
$(r-i)_{RC,0}$	0.290 ± 0.041 mag
$m_{g,RC,0}$	15.810 ± 0.056 mag
$m_{r,RC,0}$	15.031 ± 0.026 mag
$m_{i,RC,0}$	14.741 ± 0.032 mag
$m_{g,RC,centroid}$	18.85 ± 0.30 mag
$m_{r,RC,centroid}$	17.01 ± 0.25 mag
$m_{i,RC,centroid}$	16.03 ± 0.24 mag
$(g-r)_{RC,centroid}$	1.87 ± 0.13 mag
$(r-i)_{RC,centroid}$	1.01 ± 0.06 mag
A_g	3.037 ± 0.056 mag
A_r	1.981 ± 0.026 mag
A_i	1.290 ± 0.032 mag
$E(g-r)$	1.091 ± 0.062 mag
$E(r-i)$	0.722 ± 0.041 mag

1.26×10^{10} yr to find the closest matching colors for each isochrone. This analysis indicated a source effective temperature of $T_{\text{eff}} = 4290.9 \pm 50.0$ K, suggesting that the source star is a K-type star.

The angular radius, θ_s , for the source star was then calculated using the relationships between the limb-darkened θ_s and stellar colors in SDSS passbands derived from Boyajian et al. (2014). Both color indices for which coefficients were published yielded consistent estimates: $\theta_{s,(g-r)} = 7.144 \pm 0.319 \mu\text{as}$ and $\theta_{s,(g-i)} = 7.431 \pm 0.232 \mu\text{as}$. We adopt an average of these two results, $\theta_s = 7.288 \pm 0.394 \mu\text{as}$.

The final required constraint is to determine the distance to the source, so that $\rho = \theta_s/\theta_E$ can be used to measure the Einstein radius. The best way to provide this constraint would be a measurement of the source's parallax from the *Gaia* mission (Gaia Collaboration et al. 2016), although its source catalog is restricted to the brightest stars only in bulge fields, owing to limitations of the on-board processing. The *Gaia* Data Release 2 catalog (Gaia Collaboration et al. 2018) reported a source (id = 4062576103277425536) within 0.185 arcsec of this event, though its parallax measurement ($0.13233847489290135 \pm 0.10027593536929187$ mas) was flagged as uncertain. The catalog of distances provided by Bailer-Jones et al. (2018) gave an ill-constrained measurement of 8342^{+12860}_{-5333} pc. It should also be borne in mind that this measurement reflects the flux of the source+blend, at baseline, and the methodology was not optimized for crowded fields.

However, the source angular radii derived from Boyajian et al. (2014) and the color indices imply that the source is a giant, and its position on the color-magnitude diagrams is consistent with a red clump giant in the bulge at a distance of 7.87 kpc, as calculated earlier. Adopting this distance for the source, we infer a radius of $12.330 \pm 0.666 R_\odot$.

Combining these quantities, with the parameters of our best-fitting model, we infer the physical properties of the lens from the following relations. The angular Einstein radius, θ_E , was extracted from the ratio of source radii ρ in Einstein and θ_s in absolute units. This quantity relates directly to the total lens mass, M_L , the lens distance, D_L , and the lens-source separation,

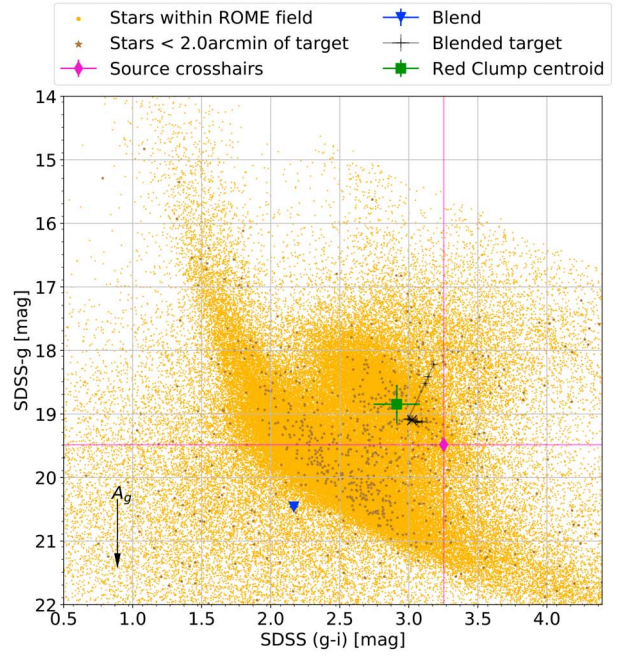
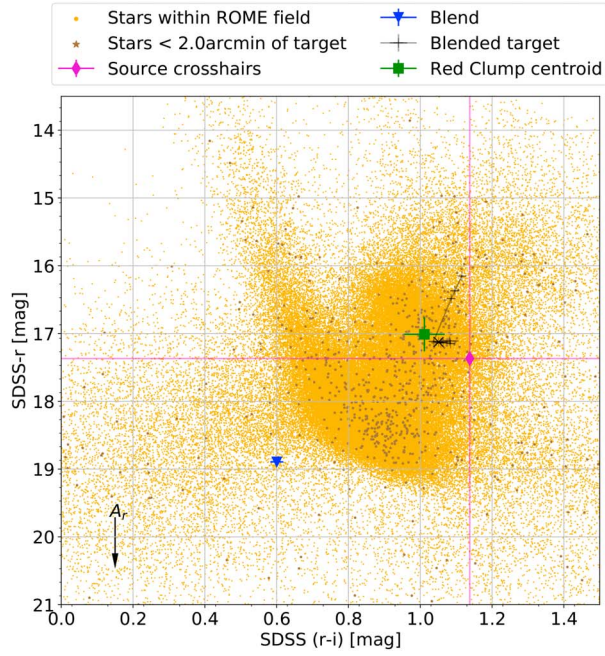


Figure 4. ROME color–magnitude diagrams for the field containing OGLE-2018-BLG-0022. Stars within 2 arcmin of the target are highlighted in dark brown, whereas stars in the rest of the field are plotted in yellow. The center of the red clump is marked with a green square, and that of the blend by a blue triangle. The magnitude of the source+blend is plotted as a function of time as black + symbols. The magenta diamond marks the location of the source, overlaid with crosshairs. An arrow indicates the extinction vector at the distance of the lens.

Table 7
Photometric Properties of the Source Star (S) and Blend (b)

$m_{g,S}$	19.484 ± 0.007 mag	$m_{g,b}$	20.462 ± 0.027 mag
$m_{r,S}$	17.369 ± 0.002 mag	$m_{r,b}$	18.895 ± 0.013 mag
$m_{i,S}$	16.231 ± 0.001 mag	$m_{i,b}$	18.294 ± 0.013 mag
$(g-r)_S$	2.115 ± 0.007 mag	$(g-r)_b$	1.567 ± 0.030 mag
$(g-i)_S$	3.253 ± 0.007 mag	$(g-i)_b$	2.168 ± 0.030 mag
$(r-i)_S$	1.138 ± 0.002 mag	$(r-i)_b$	0.601 ± 0.018 mag
$m_{g,S,0}$	16.447 ± 0.056 mag		
$m_{r,S,0}$	15.388 ± 0.026 mag		
$m_{i,S,0}$	14.941 ± 0.032 mag		
$(g-r)_{S,0}$	1.059 ± 0.007 mag		
$(g-i)_{S,0}$	1.506 ± 0.007 mag		
$(r-i)_{S,0}$	0.447 ± 0.002 mag		

D_{LS} ,

$$\theta_E = \frac{\theta_S}{\rho} = \sqrt{\frac{4GM_L}{\mu D_L c^2}}, \quad (6)$$

$$\mu = 1 + \frac{D_L}{D_{LS}}. \quad (7)$$

The distance to the lens was inferred from the relative parallax, π_{rel} , determined from our best-fit model, and the parallax to the source, π_S ,

$$\pi_L = \pi_{\text{rel}} + \pi_S, \quad (8)$$

$$\pi_S = 1 \text{ au}/D_S, \quad (9)$$

$$D_L = 1 \text{ au}/\pi_L. \quad (10)$$

The resulting lens properties are summarized in Table 8. The lens masses are consistent with a low-mass stellar binary composed of an M6-7 star orbiting an M3 star.

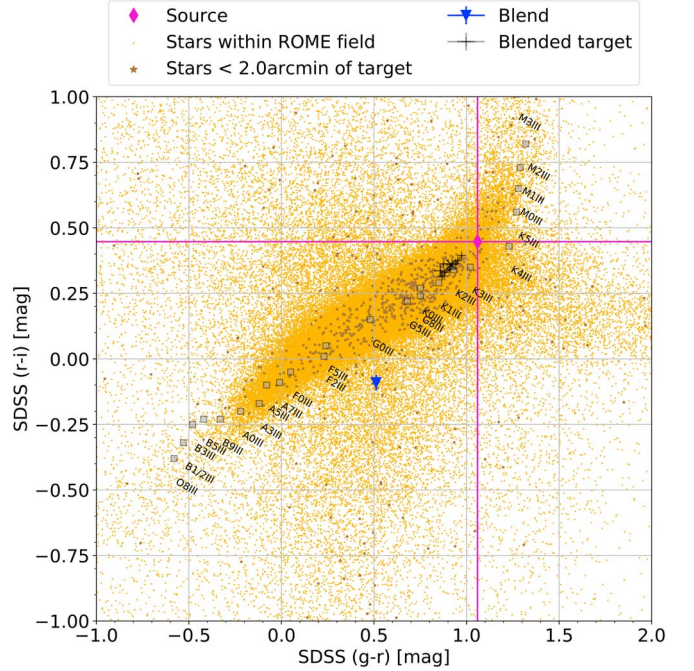


Figure 5. ROME color–color diagram for the field containing OGLE-2018-BLG-0022. Stars within 2 arcmin of the target are highlighted in dark brown, whereas stars in the rest of the field are plotted in yellow. The location of the source is indicated by a magenta diamond, and that of the blend with a blue triangle. The magnitude of the source+blend is plotted as a function of time as black + symbols. The overlaid colors of the giant sequence was derived from Pickles (1998) and plotted for comparison.

7. Assessment of the Lens and Blended Flux

The lensing system in this case is relatively close, compared with other microlensing discoveries, and its location suggests

Table 8
Physical Properties of the Source and Lens System

Parameter	Units	Value
θ_S	μas	7.288 ± 0.394
θ_E	μas	1837.145 ± 99.384
R_S	R_\odot	12.327 ± 0.666
$M_{L,\text{tot}}$	M_\odot	0.473 ± 0.026
$M_{L,1}$	M_\odot	0.376 ± 0.020
$M_{L,2}$	M_\odot	0.098 ± 0.005
D_L	Kpc	0.998 ± 0.047
a_\perp	au	0.967 ± 0.070
μ	mas yr^{-1}	8.96 ± 0.48

Table 9
Predicted Photometric Properties of the Lens System

Quantity (mag)	M3-dwarf	M7-dwarf	MS-binary M3+M7
M_B	13.175	21.124	13.174
M_V	11.574	18.674	11.572
M_g	11.933	19.149	11.932
M_r	10.409	17.181	10.407
M_i	9.475	14.700	9.466
M_J	7.566	11.033	7.522
M_H	7.014	10.458	6.969
M_{Ks}	6.779	10.178	6.733
$(B - V)$	1.601	2.450	1.602
$(g - r)$	1.524	1.968	1.525
$(r - i)$	0.934	2.481	0.941
$(J - H)$	0.552	0.575	0.553
$(H - Ks)$	0.235	0.280	0.237
$(J - Ks)$	0.787	0.855	0.790
m_B	23.169	31.118	23.168
m_V	21.568	28.668	21.566
m_g	21.927	29.143	21.926
m_r	20.403	27.175	20.401
m_i	19.469	24.694	19.460
m_J	17.560	21.027	17.516
m_H	17.008	20.452	16.963
m_{Ks}	16.773	20.172	16.727
$m_{V,\text{corr}}$	22.155	29.255	22.153
$(B - V)_{\text{corr}}$	1.836	2.685	1.837
$m_{g,\text{corr}}$	22.778	29.994	22.777
$m_{r,\text{corr}}$	20.935	27.707	20.933
$m_{i,\text{corr}}$	19.851	25.076	19.842
$(g - r)_{\text{corr}}$	1.843	2.287	1.844
$(r - i)_{\text{corr}}$	1.084	2.631	1.091

Note. Apparent magnitudes are calculated for the measured lens distance without extinction or reddening, except for the bottom section.

that the binary may lie in the Galactic disk. Given the measured masses, the simplest explanation is that the lens consists of two main-sequence components. However, we noted that, with a distance modulus of 9.99 ± 0.47 mag, a main-sequence binary might be detectable, and we estimated its likely photometric properties as follows.

We extracted the absolute magnitudes of M-type stars from a PARSEC isochrone, assuming solar age and metallicity, and calculated the expected apparent magnitudes of the binary

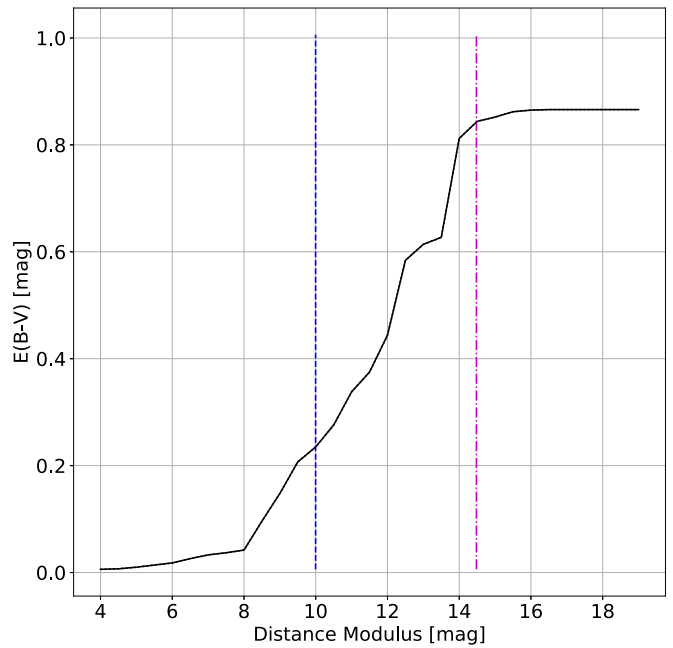


Figure 6. Color excess as a function of distance modulus along the line of sight to OGLE-2018-BLG-0022, derived from the 3D extinction maps published by Green et al. (2015). The purple dashed-dotted line marks the distance modulus of the source star while the blue dashed line indicates that of the lens.

at the lens distance (see Table 9). These magnitudes are significantly brighter than the limiting magnitude of the ROME data (limited by the sky background, ~ 21.969 mag [SDSS-*g*], ~ 21.989 mag [SDSS-*r*], ~ 22.010 mag [SDSS-*i*]), and suggest that the lens could be contributing to the blend flux we measured from the light curve.

Before drawing any conclusions however, extinction and reddening must be considered. Data from the Pan-STARRS1 (Chambers et al. 2016) and 2MASS (Skrutskie et al. 2006) surveys have been combined to provided maps of the 3D reddening within the Milky Way (Green et al. 2015), which we can use to estimate this quantity along the line of sight to the source star in this event. By interpolating the data at the (l, b) of this event, we estimated the color excess to the lens star to be $E(B - V) = 0.235 \pm 0.032$ mag (Figure 6). This was used to estimate the extinction in *V*-band, $A_V = R_V E(B - V)$, where the reddening, R_V , was estimated for the Galactic bulge by Nataf et al. (2013) to be $\sim 2.5 \pm 0.2$. We therefore found $A_V = 0.59 \pm 0.09$ mag. This was used to estimate the extinction in Sloan filters by applying the transforms derived by Schlafly & Finkbeiner (2011), interpolating between the discrete values of R_V they provided to arrive at extinction values for this field of $A_{(\text{SDSS}-g)} = 0.851 \pm 0.118$ mag, $A_{(\text{SDSS}-r)} = 0.532 \pm 0.074$ mag, $A_{(\text{SDSS}-i)} = 0.382 \pm 0.053$ mag. The extinction-corrected apparent magnitudes for the lens binary scenario are presented at the bottom of Table 9.

The measured blend photometry in Table 7 indicates one or more objects that are significantly brighter than the photometry predicted for a main-sequence M3+M7 binary, implying that the light originates from a separate object(s)—a common situation in the crowded star fields of the Galactic bulge. Nevertheless, we note that the lens should be easily detectable in 2–4 m class telescopes, particularly in the near-infrared.

8. Conclusions

The microlensing event OGLE-2018-BLG-0022 revealed the presence of an M3+M7 binary star, previously undetected owing to its intrinsically low luminosity. That said, the binary in this event is unusually close to the Earth for a microlens— ~ 1 kpc away—and the object shows a correspondingly high relative proper motion of 8.96 mas yr^{-1} . This makes it a good candidate for high spatial resolution adaptive optics imaging in the relatively near future which, as discussed by Henderson et al. (2014), could provide an independent verification of the lens mass determination. While the proximity of the lens, resulting in a large (1.84 mas) angular Einstein radius, would have been resolvable to interferometry, as demonstrated by Dong et al. (2019), the source star in this case was too faint for current instruments. The discovery highlights microlensing's capability to map populations beyond the solar neighborhood that would otherwise be hidden by their intrinsically faint luminosities.

R.A.S. and E.B. gratefully acknowledge support from NASA grant NNX15AC97G. Y.T. and J.W. acknowledge the support of DFG priority program SPP 1992 Exploring the Diversity of Extrasolar Planets (WA 1047/11-1). K.H. acknowledges support from STFC grant ST/R000824/1. This research has made use of NASA's Astrophysics Data System, and the NASA Exoplanet Archive. The work was partly based on data products from observations made with ESO Telescopes at the La Silla Paranal Observatory under programme ID 177. D-3023, as part of the VST Photometric Halpha Survey of the Southern Galactic Plane and Bulge (VPHAS+; www.vphas.eu). This work also made use of data from the European Space Agency (ESA) mission *Gaia* (<https://www.cosmos.esa.int/gaia>), processed by the *Gaia* Data Processing and Analysis Consortium (DPAC; <https://www.cosmos.esa.int/web/gaia/dpac/consortium>). Funding for the DPAC has been provided by national institutions, in particular the institutions participating in the *Gaia* Multilateral Agreement. CITEUC is funded by National Funds through FCT—Foundation for Science and Technology (project: UID/Multi/00611/2013) and FEDER—European Regional Development Fund through COMPETE 2020 Operational Programme Competitiveness and Internationalization (project: POCI-01-0145-FEDER-006922). The work by S.S. and S.R. was supported by a grant (95843339) from the Iran National Science Foundation (INSF). D.M.B. acknowledges the support of the NYU Abu Dhabi Research Enhancement Fund under grant RE124. This research uses data obtained through the Telescope Access Program (TAP), which has been funded by the National Astronomical Observatories of China, the Chinese Academy of Sciences, and the Special Fund for Astronomy from the Ministry of Finance. This work was partly supported by the National Science Foundation of China (grant No. 11333003, 11390372 and 11761131004 to S.M.).

ORCID iDs

R. A. Street  <https://orcid.org/0000-0001-6279-0552>
 K. Horne  <https://orcid.org/0000-0003-1728-0304>
 Weicheng Zang  <https://orcid.org/0000-0001-6000-3463>

References

- Albrow, M. D., Beaulieu, J.-P., Caldwell, J. A. R., et al. 1999, *ApJ*, 522, 1022
 Bachelet, E., Bramich, D. M., Han, C., et al. 2015, *ApJ*, 812, 136
 Bachelet, E., Norbury, M., Bozza, V., & Street, R. 2017, *AJ*, 154, 203
 Bailer-Jones, C. A. L., Rybizki, J., Fouesneau, M., Mantelet, G., & Andrae, R. 2018, *AJ*, 156, 58
 Bond, I. A., Abe, F., Dodd, R. J., et al. 2001, *MNRAS*, 327, 868
 Boyajian, T. S., van Belle, G., & von Braun, K. 2014, *AJ*, 147, 47
 Bozza, V. 2010, *MNRAS*, 408, 2188
 Bozza, V., Bachelet, E., Bartolici, F., et al. 2018, *MNRAS*, 479, 5157
 Bramich, D. M. 2008, *MNRAS*, 386, L77
 Bramich, D. M. 2018, *A&A*, 618, A44
 Bramich, D. M., Horne, K., Albrow, M. D., et al. 2013, *MNRAS*, 428, 2275
 Branch, M. A., Coleman, F. T., & Li, Y. 1999, *SIAM Journal on Scientific Computing*, 21, 12
 Bressan, A., Marigo, P., Girardi, L., et al. 2012, *MNRAS*, 427, 127
 Brown, T. M., Baliber, N., Bianco, F. B., et al. 2013, *PASP*, 125, 1031
 Cao, L., Mao, S., Nataf, D., Rattenbury, N. J., & Gould, A. 2013, *MNRAS*, 434, 595
 Chambers, K. C., Magnier, E. A., Metcalfe, N., et al. 2016, arXiv:1612.05560
 Claret, A., & Bloemen, S. 2011, *A&A*, 529, A75
 Coleman, F. T., & Li, Y. 1994, *MatPr*, 67, 189
 Dominik, M. 1999, *A&A*, 349, 108
 Dominik, M. 2009, *MNRAS*, 393, 816
 Dominik, M., Horne, K., Allan, A., et al. 2008, *AN*, 329, 248
 Dominik, M., Jørgensen, U. G., Rattenbury, N. J., et al. 2010, *AN*, 331, 671
 Dominik, M., Rattenbury, N. J., Allan, A., et al. 2007, *MNRAS*, 380, 792
 Dong, S., Mérand, A., Delplancke-Ströbele, F., et al. 2019, *ApJ*, 871, 70
 Dong, S., Udalski, A., Gould, A., et al. 2007, *ApJ*, 664, 862
 Drew, J. E., Gonzalez-Solares, E., Greimel, R., et al. 2014, *MNRAS*, 440, 2036
 Evans, D. F., Southworth, J., Maxted, P. F. L., et al. 2016, *A&A*, 589, A58
 Foreman-Mackey, D., Hogg, D. W., Lang, D., & Goodman, J. 2013, *PASP*, 125, 306
 Gaia Collaboration, Brown, A. G. A., Vallenari, A., et al. 2018, *A&A*, 616, A1
 Gaia Collaboration, Prusti, T., de Bruijne, J. H. J., et al. 2016, *A&A*, 595, A1
 Green, G. M., Schlafly, E. F., Finkbeiner, D. P., et al. 2015, *ApJ*, 810, 25
 Henderson, C. B., Park, H., Sumi, T., et al. 2014, *ApJ*, 794, 71
 Hundertmark, M., Street, R. A., Tsapras, Y., et al. 2018, *A&A*, 609, A55
 Levenberg, K. 1944, *QApMa*, 2, 164
 Marquardt, D. 1963, *J. Appl. Math.*, 11, 431
 Minniti, D., Lucas, P. W., Emerson, J. P., et al. 2010, *NewA*, 15, 433
 Nataf, D. M., Gould, A., Fouqué, P., et al. 2013, *ApJ*, 769, 88
 Park, B.-G., Kim, S.-L., Lee, J. W., et al. 2012, *Proc. SPIE*, 8444, 844447
 Pickles, A. J. 1998, *PASP*, 110, 863
 Refsdal, S. 1964, *MNRAS*, 128, 295
 Ruiz-Dern, L., Babusiaux, C., Arenou, F., Turon, C., & Lallement, R. 2018, *A&A*, 609, A116
 Sako, T., Sekiguchi, T., Sasaki, M., et al. 2008, *ExA*, 22, 51
 Saunders, E. S., Lampoudi, S., Lister, T. A., Norbury, M., & Walker, Z. 2014, *Proc. SPIE*, 9149, 91490E
 Schlafly, E. F., & Finkbeiner, D. P. 2011, *ApJ*, 737, 103
 Shvartzvald, Y., Bryden, G., Gould, A., et al. 2017, *AJ*, 153, 61
 Shvartzvald, Y., Li, Z., Udalski, A., et al. 2016, *ApJ*, 831, 183
 Skottfelt, J., Bramich, D. M., Hundertmark, M., et al. 2015, *A&A*, 574, A54
 Skowron, J., Shin, I. G., Udalski, A., et al. 2015, *ApJ*, 804, 33
 Skrutskie, M. F., Cutri, R. M., Stiening, R., et al. 2006, *AJ*, 131, 1163
 Storn, R., & Price, K. 1997, *J. Global Optim.*, 11, 341
 Sumi, T., Abe, F., Bond, I. A., et al. 2003, *ApJ*, 591, 204
 Sumi, T., & Penny, M. T. 2016, *ApJ*, 827, 139
 Udalski, A., Szymanski, M., Kaluzny, J., Kubiak, M., & Mateo, M. 1992, *AcA*, 42, 253
 Wegg, C., & Gerhard, O. 2013, *MNRAS*, 435, 1874
 Wyrzykowski, Z., Kostrzewa-Rutkowska, J., Skowron, K. A., et al. 2016, *MNRAS*, 458, 3012